Locking Orbital Angular Momentum with Linear Momentum of Light

Hui-Ming Wang,[1,2,*] Yuan Chen,[3,*] Ming-Yuan Chen,[4,*] Ying-Yu Fang,[1,2] Ka-Di Zhu,[5,†] Cheng-Wei Qiu,[6,‡] Yan-Qing Lu,[4,§] Keyu Xia,[2,4,7,‖] and Xian-Min Jin[1,2,8,9,¶]

[1]*Center for Integrated Quantum Information Technologies (IQIT), School of Physics and Astronomy and State Key Laboratory of Photonics and Communications, Shanghai Jiao Tong University, Shanghai 200240, China*

[2]*Hefei National Laboratory, Hefei 230088, China*

[3]*International Quantum Academy, Shenzhen 518048, China*

[4]*College of Engineering and Applied Sciences, National Laboratory of Solid State Microstructures, Nanjing University, Nanjing 210023, China*

[5]*Key Laboratory of Artificial Structures and Quantum Control (Ministry of Education) and School of Physics and Astronomy, Shanghai Jiao Tong University, Shanghai 200240, China*

[6]*Department of Electrical and Computer Engineering, National University of Singapore, Singapore 117583, Singapore*

[7]*Shishan Laboratory, Suzhou Campus of Nanjing University, Suzhou 215000, China*

[8]*TuringQ Co., Ltd., Shanghai 200240, China*

[9]*Chip Hub for Integrated Photonics Xplore (CHIPX), Shanghai Jiao Tong University, Wuxi 214000, China*

(Received 10 March 2025; revised 15 May 2025; accepted 23 June 2025; published 2 October 2025)

Correlation between the propagation direction of light and spin can be induced via the spin-orbit interaction and has been proven to be the workhorse in the emerging field of chiral quantum optics and in the spin-related Hall effects of light. Photonic orbital angular momentum (OAM) provides a high-dimensional degree of freedom in classical and quantum information processing. However, integrated OAM-based information technology is an open challenge, because OAM modes are always generated in pairs with opposite topological charges due to their degeneracy. Here, we observe locking of the OAM and linear momentum of light by using a chiral optical waveguide with an Archimedean cross section to induce the orbit-orbit interaction. This OAM-momentum locking enables the deterministic and robust generation of on-demand OAM vortex light beam in a photonic chip. This new correlation paves the way toward exotic high-dimensional chiral physical effects and also provides the capability of on-chip manipulation of light in high-dimensional space.

DOI: 10.1103/tttd-v936

Introduction—The direction of propagation (longitudinal linear momentum, also namely orbit), spin angular momentum, and orbital angular momentum (OAM) of flying photons are typically decoupled in a medium. The interaction between these momenta is of paramount importance for manipulating photons and has been intensively studied for fundamental physics and exotic applications. Strikingly, the transverse spin of light in a photonic microstructure can couple to the longitudinal linear momentum [1–5], namely, the spin-orbit interaction. It can result in the so-called spin-momentum locking and is one of the cornerstones for topological photonics [3,6,7]. The spin-momentum locking has stimulated the birth of the field of chiral quantum optics [1,8–11] and, thus, plays the role of workhorse [12–15]. It is also the key mechanism of numerous spin-related Hall effects of light [2,3,12,16–18], quantum nonreciprocity [4,5,19,20], directional emission of photons in diverse microstructures [10,18,21–24], and the high-dimensional OAM microlaser [25,26].

Besides the spin angular momentum, a light beam can also possess two types of angular momenta: the external OAM arose from the spiral light trajectory, and the intrinsic OAM caused by the spiral phase $\exp(i\ell\varphi)$, with ℓ being topological charge and φ the azimuthal phase. Below, we refer to OAM as the intrinsic OAM. Since the light carrying OAM was conceptually revealed [27,28], the OAM of photons provides an ideal carrier for high-dimensional information technologies [29–35]. On-chip generation of a pure vortex light beam with a selected OAM is highly demanded for large-scale OAM-based high-dimensional information processing [36–42]. Meanwhile, exploration of the coupling of OAMs and other degrees of freedom of light can deepen our understanding of the fundamental nature of photonic OAMs and pave a cornerstone for

*These authors contributed equally to this work.
†Contact author: zhukadi@sjtu.edu.cn
‡Contact author: chengwei.qiu@nus.edu.sg
§Contact author: qylu@nju.edu.cn
‖Contact author: keyu.xia@nju.edu.cn
¶Contact author: xianmin.jin@sjtu.edu.cn

studying high-dimensional light-matter interactions [43]. Despite great success, it is still a challenging task to selectively generate an OAM vortex light beam with high fidelity in a photonic chip, because a photonic microstructure is degenerate thus far for the OAM modes with opposite topological charges $\pm\ell$. Like the directional emission of a photon enabled by spin-momentum locking, the on-chip orbit-orbit interaction (OOI) and the resultant OAM-momentum locking of light in a photonic microstructure may open a door for this task but have not been reported yet. Here, the OOI means the coupling between the OAM and longitudinal linear momentum of light.

In this Letter, we create the OOI of light and experimentally lift the $\pm\ell$ degeneracy with a laser-direct-written chiral photonic circuit. Based on the broken degeneracy, we experimentally observe OAM-momentum locking and, thus, the generation of an OAM mode with on-demand topological charge in a photonic chip. Benefit to OAM-momentum locking, the generation of vortex light beams is robust against structure variations. As spin-momentum locking, this OAM-momentum locking fills a missing part for exploring OAMs for chiral optics. Even beyond, this mechanism offers significant advantages in leveraging OAMs for on-chip high-dimensional information processing [44,45].

Theory of OAM-momentum locking—The concept underpinning our chiral waveguide for creating the OAM-momentum locking is schematically explained in Fig. 1. The waveguides can be fabricated in a photonic chip by the laser direct writing technique. An optical waveguide with a Gaussian refractive index distribution in cross section only supports the propagation of Gaussian modes of light with zero topological charge, i.e., $\ell = 0$. Two nearby Gaussian waveguides form a standard direction coupler [Fig. 1(a)]. The Gaussian modes of light can transfer between the two waveguides without phase mismatching in opposite directions over a wide wave number range [Fig. 1(d)]. A doughnut-shaped OAM waveguide can guide a pair of degenerate OAM modes with selected opposite topological charges $\pm\ell$ in each direction [Fig. 1(b)] [46]. As is shown in Fig. 1(e), light in a Gaussian waveguide can excite $\pm\ell$ modes in a doughnut-shaped OAM waveguide; this is because the phase matching condition is satisfied for both $\pm\ell$ topological charges, i.e., $\delta\beta_{|\ell|} = 0$. As a benchmark of this Letter, we theoretically propose a chiral waveguide with an Archimedean spiral (AS) refractive index profile for inducing OAM-momentum locking [Fig. 1(c)]. The helicity of such a waveguide is dependent on the propagation direction of light, breaking the mirror symmetry. Thus, this waveguide is chiral and lifts the degeneracy of the propagation constant of the $\pm\ell$ modes [Fig. 1(f)], leading to OAM-momentum locking. Experimentally, this locking is manifested in the direction coupler by the observation that a Gaussian mode with $k_z = k_0$ ($k_z = -k_0$) can excite only the $+\ell$ ($-\ell$) OAM mode, because $\delta\beta_{+\ell} = 0$ but $\delta\beta_{-\ell} \neq 0$ ($\delta\beta_{-\ell} = 0$ but $\delta\beta_{+\ell} \neq 0$). Below, we denote

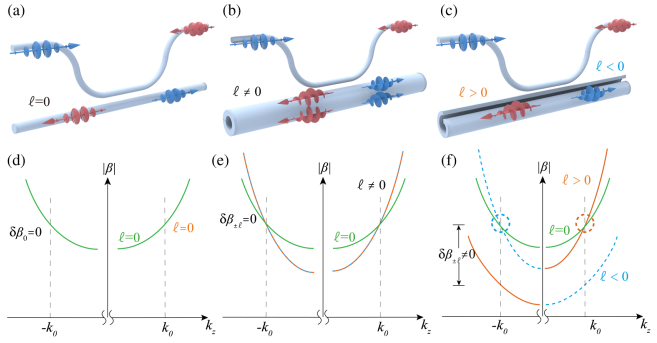

FIG. 1. Schematics of three types of directional couplers and corresponding phase matching conditions. (a) The standard direction coupler composing of two Gaussian waveguides supporting Gaussian modes with $\ell = 0$. (b) A direction coupler composing of a Gaussian waveguide and an doughnut-shaped OAM waveguide, which guides the nonzero $\pm\ell$ modes with a degenerate propagation constant. (c) A direction coupler made from a Gaussian waveguide and a chiral waveguide with an Archimedean spiral refractive index profile. The chiral waveguide lifts the degeneracy of the $\pm\ell$ modes and exhibits OAM-momentum locking. (d)–(f) show phase matching of the propagation constant β of light in two waveguides, corresponding to couplers in (a)–(c). In (a) and (d), light in the two waveguides is always in phase matching. In (b) and (e), a pair of selected $\mathrm{OAM}_{+\ell}$ and $\mathrm{OAM}_{-\ell}$ modes can be simultaneously excited when phase matching is met at $k_z = k_0$ or $k_z = -k_0$, because they are degenerate in propagation constant β. (c),(f) The degeneracy of the $\mathrm{OAM}_{+\ell}$ and $\mathrm{OAM}_{-\ell}$ modes is lifted in the chiral waveguide, i.e., $\delta\beta_{+\ell} \neq \delta\beta_{-\ell}$; the topological charge and momentum are correlated.

an OAM mode with topological charge ℓ as OAM_ℓ for simplicity.

The chiral waveguide is experimentally fabricated by the laser direct writing technique. We show the chiral waveguide supporting $\mathrm{OAM}_{\pm1}$ and $\mathrm{OAM}_{\pm2}$ modes in Fig. 2. Each chiral waveguide composes of 12 subwaveguides with centers at radial coordinate ρ_0. The centers are arranged along an Archimedean spiral curve defined as $\rho_0 = a_{|\ell|} + \mathrm{sgn}(k_z) b_{|\ell|}\varphi$ in the polar coordinates (ρ, φ, z), where $\varphi \in [0, 2\pi)$, $a_{|\ell|}$ stands for the beginning point of the spiral curve, $b_{|\ell|}$ controls the degree of helicity of the chiral waveguide, and k_z represents the longitudinal momentum of light along the positive z axis. Specifically, the 12 subwaveguides are arranged with an equal angular interval from $\varphi = \pi/6$ to 2π. The cross section of each subwaveguide approximately has a Gaussian-distributed relative dielectric constant $\varepsilon(\mathbf{r})$ as follows:

$$\varepsilon(\mathbf{r}) = \delta\varepsilon_0 e^{-(\rho-\rho_0)^2/\delta\rho^2} + \varepsilon_s, \tag{1}$$

where ε_s is the relative dielectric constant of material, $\delta\varepsilon_0$ is the modification induced by laser writing, and $\delta\rho$ describes the width of Gaussian distribution of the relative dielectric constant. In the experiment, we have $\delta\varepsilon_0/\varepsilon_s \sim 10^{-3} - 10^{-4}$. Here, $\varepsilon(\mathbf{r})$ is a constant in the z direction and, thus, can be replaced with $\varepsilon(\rho, \varphi)$.

By setting $V(\mathbf{r}) \equiv \ln[\varepsilon(\mathbf{r})]$ as an effective potential and considering the eigenmode with frequency ω, photons propagating along the chiral waveguide can be described by the time-independent Schrödinger-like wave equation with eigenvalue β^2 [47,48]:

$$\begin{aligned}(\hat{H}_0 + \hat{H}')|\psi\rangle &= \beta^2|\psi\rangle, \\ \hat{H}_0|\psi\rangle &= [\nabla_T^2 + k^2(\rho,\varphi)]|\psi\rangle, \\ \hat{H}'|\psi\rangle &= \nabla_T[|\psi\rangle \cdot \nabla_T V(\rho,\varphi)]\end{aligned} \tag{2}$$

with Hamiltonian-like unperturbed operator $\hat{H}_0$ and perturbation operator $\hat{H}'$, transverse gradient operator ∇_T, and Laplacian ∇_T^2, $k^2(\rho,\varphi) = \varepsilon(\rho,\varphi)\omega^2/c^2$, where c is the speed of light in vacuum, β is the longitudinal propagation constant, and wave function for the eigenmode $|\psi\rangle = \mathbf{e}_\sigma \psi_{n|\ell|}(\rho,\varphi)e^{i\ell\varphi+i\beta z}$ in the cylindrical coordinate system (see Supplemental Material, Sec. II [49]). The dimensionless scalar function $\psi_{n|\ell|}(\rho,\varphi)$ is determined by $k^2(\rho,\varphi)$, and $\mathbf{e}_\sigma$ is the unit vector of the polarization.

We can assume that the unperturbed Hamiltonian $\hat{H}_0$ has an eigenvalue β_0^2. The perturbation term $\hat{H}'|\psi\rangle$ includes OOI

$$\hat{H}_{\mathrm{OM}} = \gamma b_{|\ell|}\hat{m}\hat{\ell}_z/\beta_0 \tag{3}$$

with strength γ, the momentum-orbital operator $\hat{m} = -i\partial_z$, and the z-component OAM-orbital operator $\hat{\ell}_z = -i\partial_\varphi$. We have $\hat{m}|\psi\rangle = \beta|\psi\rangle$ and $\hat{\ell}|\psi\rangle = \ell|\psi\rangle$. This interaction gives rise to ℓ- and k_z-dependent correction to the propagation constant β_0, lifting the $\pm\ell$ degeneracy and leading to OAM-momentum locking. This OOI is the origin of the optical Magnus effect [52].

To study the effect of OOI, we replace β with $\beta_{\ell_k} = \beta_0 + \delta\beta_{\ell_k}$ and $\delta\beta_{\ell_k}$ being the propagation constant shift from β_0. We introduce the notation $\ell_k \equiv |\ell|\mathrm{sgn}(\ell \cdot k_z)$. Using $k_z \approx \beta_0$, the first-order correction to propagation constant is

$$\delta\beta_{\ell_k} = \gamma b_{|\ell|}\ell_k. \tag{4}$$

The effective propagation constant β_{ℓ_k} is critically dependent on the topological charge ℓ, the structure parameter $b_{|\ell|}$, and the momentum k_z of photons (see Supplemental Material, Sec. II [49]). Obviously, the propagation-constant degeneracy breaks for OAM modes with opposite ℓ propagating in the same direction and, therefore, causes OAM-momentum locking. In the OAM emitter, a single vortex beam is excited only when the phase matching condition between the OAM_ℓ mode and the Gaussian input mode is satisfied. It is worthy noting that the phase matching is met only for paired ℓ and k_z. Thus, the OAM_ℓ and $\mathrm{OAM}_{-\ell}$ modes can be generated only in opposite directions. This $\ell - k_z$-paired excitation of OAM modes definitely reflects OAM-momentum locking and opens a new door for conducting chiral photonics in high-dimensional space.

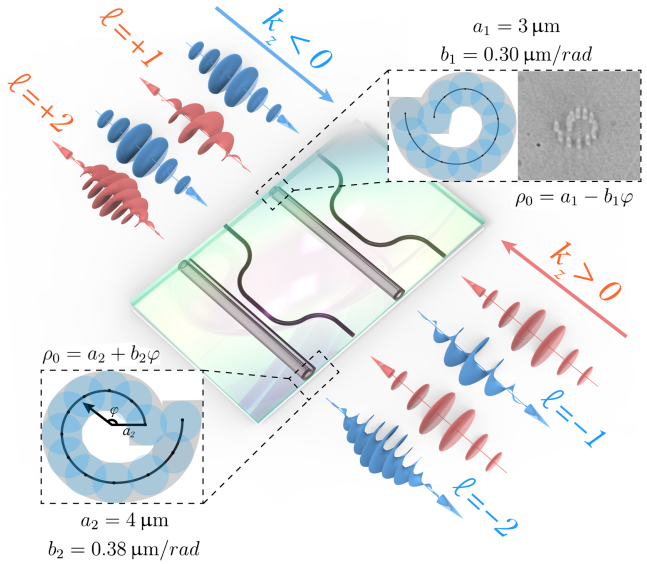

FIG. 2. Experimental chiral OAM emitters. First-order ($|\ell| = 1$) and second-order ($|\ell| = 2$) OAM mode emitters consisting of a curved single-mode waveguide and a chiral waveguide. A positive (negative) wave vector $k_z > 0$ ($k_z < 0$), marked as a red (blue) arrow, indicates a Gaussian beam incident to the left (right) end of the single-mode waveguide. The correspondingly generated OAM mode with positive (negative) topological charge is marked with a red (blue) spiral wave front. The bottom-left inset shows the ideal cross section of a chiral waveguide for $|\ell| = 2$. The top-right inset shows the ideal cross section of the chiral waveguide for $|\ell| = 1$ and the experimental cross-section image as an example.

Experimental observation of OAM-momentum locking—Experimentally, the chiral OAM emitter is schematically shown in Fig. 2. A Gaussian-mode input waveguide and an AS waveguide embedded in the photonic chip form an ℓ-selective emitter. The insets, respectively, show the ideal schematic and experimentally measured microscopic images of spiral cross sections. The black dots along the spiral curves on the ideal cross section indicate the centers of the writing laser focus (see Supplemental Material, Sec. I [49]). The helicity of the OAM waveguide with fixed parameters $a_{|\ell|}$ and $b_{|\ell|}$ can be either counterclockwise or clockwise, depending on the observing direction $\mathrm{sgn}(k_z)$. By properly choosing parameters $a_{|\ell|}$ and $b_{|\ell|}$ so that the phase matching condition between the Gaussian and AS waveguides is satisfied, one can selectively excite an OAM mode with a specific topological charge ℓ.

As the theoretical discussion based on Figs. 1 and 2, the OOI in the AS waveguide breaks the degeneracy of OAM modes with opposite topological charges and induces OAM-momentum locking. As a result, when a Gaussian beam with $\ell = 0$ is incident on the input waveguide,

a vortex OAM beam with selective topological charge ℓ_{out} can be emitted from the output end of the AS waveguide. The topological charge of the outgoing vortex beam is determined by structure parameters of the AS waveguide and the longitudinal momentum of light k_z. For a Gaussian beam input to the left side ($k_z < 0$), the topological charge of the emitted vortex beam is negative, i.e., $\ell_{\text{out}} < 0$. When the input direction reverses ($k_z > 0$), the emitted vortex beam has $\ell_{\text{out}} > 0$, because the helicity of the AS waveguide changes from counterclockwise to clockwise. By adjusting parameters $a_{|\ell|}$ and $b_{|\ell|}$, we can tune the orders of vortex OAM beams on demand. Taking $a_1 = 3$ μm and $b_1 = 0.30$ μm/rad, the emitted vortex beam has $\ell_{\text{out}} = -1$ for $k_z < 0$ and $\ell_{\text{out}} = 1$ for $k_z > 0$. As an example, increasing parameters $a_{|\ell|}$ and $b_{|\ell|}$ to $a_2 = 4$ μm and $b_2 = 0.38$ μm/rad, the topological charge becomes $\ell_{\text{out}} = -2$ for $k_z < 0$ and $\ell_{\text{out}} = 2$ for $k_z > 0$. In principle, we can fabricate an OAM_ℓ waveguide supporting much higher topological charge and, thus, explore on-chip OAM emitters with tunability.

Figure 3 provides a proof-of-principle experimental observation of the theoretically predicted OAM-momentum locking. Unlike the conventional doughnut-shaped waveguide, the OOI in the chiral AS waveguide causes a nonzero shift $\delta\beta_\ell$ with $|\ell| = 1$ or 2. The sign of ℓ depends on the propagation direction k_z of the input Gaussian mode. This propagation-constant shift breaks the $\pm\ell$ degeneracy and leads to OAM-momentum locking. In experiment, the shifts $\delta\beta_1$ and $\delta\beta_2$ are positive for an input with $k_z = k_0 > 0$, as schematically shown in Fig. 1(f). The OAM_{+1} and OAM_{+2} modes, respectively, meet the phase matching condition with the input Gaussian mode in two different photonic circuits and, thus, are selectively excited. For an opposite input $k_z = -k_0$, OAM_{-1} and OAM_{-2} modes are excited.

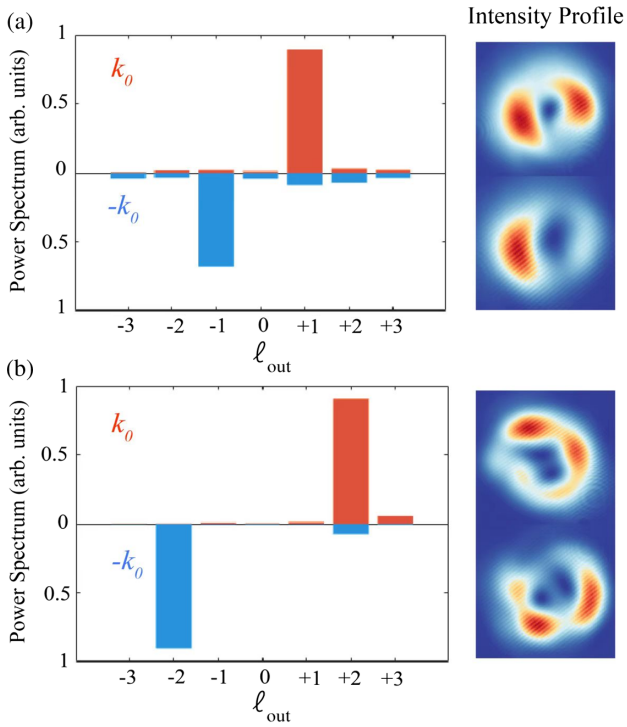

FIG. 3. Experimental observation of emitted OAM_ℓ modes. (a),(b) Power spectrum of the emitted first-order ($|\ell| = 1$) and second-order ($|\ell| = 2$) OAM modes for right-handed (orange bars) and left-handed (blue bars) inputs to the Gaussian waveguide. The column on the right shows the intensity profiles of the OAM states corresponding to the power spectrum.

The aforementioned OAM-momentum locking is clearly characterized by the selectively generation of OAM modes; see Fig. 3. To identify the emitted OAM vortex beams, we use the spatial light modulator to make projection measurement (See Supplemental Material, Sec. III [49]). Specifically, we switch the hologram applied to the spatial light modulator from $\ell_{\text{out}} = -3$ to $\ell_{\text{out}} = +3$ for measuring the power spectra of OAM modes with different ℓ_{out}. For $k_z = k_0$ ($k_z = -k_0$), taking the above-mentioned first-order OAM waveguide as an example, the measured power spectra verifies that the $\ell_{\text{out}} = +1$ ($\ell_{\text{out}} = -1$) mode is mostly excited with power proportion 89% (76%), corresponding to the purity; see Fig. 3(a). When we tune the OAM waveguide parameters, the emitter generates the OAM_{+2} (OAM_{-2}) mode with purity 87% (87%); see Fig. 3(b).

It is worth noting that the propagation-constant shift is proportional to the topological charge ℓ; see Eq. (4). Thus, $|\delta\beta_2|$ is about twice $|\delta\beta_1|$, leading to stronger OAM-momentum locking for larger $|\ell|$. This is proved by an overall higher purity of the generated $\text{OAM}_{\pm2}$ mode and the ratio between target modes and unwanted modes in the $\text{OAM}_{\pm2}$ waveguide, compared with the $\text{OAM}_{\pm1}$ waveguide.

Robustness against imperfection—The previous OAM emitters fabricated by femtosecond laser exhibit high sensitivity to machining parameters. By lifting the degeneracy of opposite OAM modes, we significantly improve the robustness of the on-chip OAM emitter here. To verify the robustness, we change the coupling length and the laser writing power and then observe the power spectra of $\text{OAM}_{\pm\ell_{\text{out}}}$ modes. The coupling length L_c varies from 3.6 to 4.4 mm with a step of 0.2 mm. We also tune the writing laser power P_w around a usable value $P_0 =$ 132.5 mW ($P_0 = 141.0$ mW), corresponding to the power for generating the $\text{OAM}_{\pm1}$ ($\text{OAM}_{\pm2}$) modes; see Figs. 4(a) and 4(b) [Figs. 4(c) and 4(d)]. The power variation, defined as $\Delta P = P_w - P_0$, ranges from 0 to 2.5 mW with an interval of about 0.6 mW (the last group is 2.5 mW). Here, we focus on the power ratio between target mode and unwanted mode. We measure 25 OAM emitters for each set of k_z and ℓ_{out}.

Figures 4(a) and 4(b) show the robust generation of the $\text{OAM}_{\ell_{\text{out}}=\pm1}$ against the variation of the coupling length and the writing laser power. The purity of target OAM modes is considerably higher than the unwanted one.

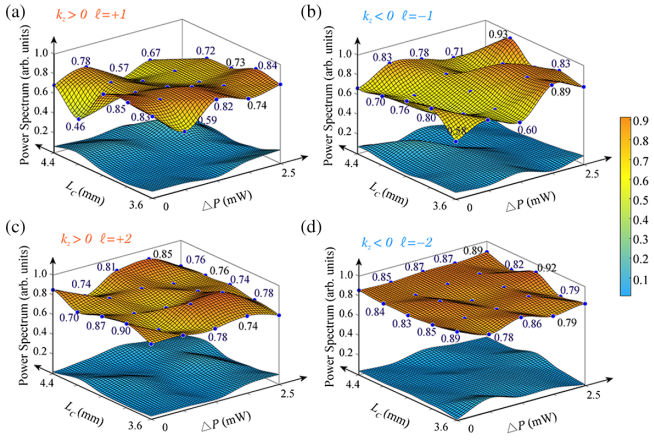

FIG. 4. Power spectra versus the writing laser power variations ΔP around a usable writing laser power P_0 and the coupling length L_c. (a) For $k_z > 0$ and $\ell_{\mathrm{out}} = 1$, the average purity is 0.72 and the standard deviation is 0.10. (b) For $k_z < 0$ and $\ell_{\mathrm{out}} = -1$, the average purity is 0.73 and the standard deviation is 0.10. (c) For $k_z > 0$ and $\ell_{\mathrm{out}} = 2$, the average purity is 0.80 and the standard deviation is 0.06. (d) For $k_z < 0$ and $\ell_{\mathrm{out}} = -2$, the average purity is 0.85 and the standard deviation is 0.03. Surfaces are fitted by experimental power proportion of 25 data points for $\ell_{\mathrm{out}} = \pm 1$ in the first-order OAM waveguide and $\ell_{\mathrm{out}} = \pm 2$ in the second-order OAM waveguide, respectively. Upper surfaces and corresponding data are for the target $\mathrm{OAM}_{\ell_{\mathrm{out}}}$ mode. Lower surfaces are fitting of the unwanted $\mathrm{OAM}_{-\ell_{\mathrm{out}}}$ mode.

For $k_z = k_0$ in Fig. 4(a), the average purity for $\ell_{\mathrm{out}} = +1$ is about 0.72. Meanwhile, the opposite OAM_{-1} mode is greatly suppressed, having only an average value of about 0.07. The average extinction ratio is about 10. When the input light momentum reverses, corresponding to the case of $k_z = -k_0$ shown in Fig. 4(b), the OAM_{-1} mode becomes dominant with an average purity of 0.73. The proportion of the suppressed OAM_{+1} mode reduces to 0.06, yielding an extinction ratio of 12.8. From a robustness perspective, the purity of target OAM modes exhibits a standard deviation of 0.10 for $\ell = +1$ and 0.10 for $\ell = -1$. The overwhelming generation of the target OAM mode clearly indicates OAM-momentum locking.

Figures 4(c) and 4(d) show the selective emission of the $\mathrm{OAM}_{\ell_{\mathrm{out}}=+2}$ ($\mathrm{OAM}_{\ell_{\mathrm{out}}=-2}$) mode for $k_z = k_0$ ($k_z = -k_0$). Because $\delta\beta_2 \sim 2\delta\beta_1$, in comparison with the $\mathrm{OAM}_{\pm 1}$ waveguide, the target second-order OAM mode has a higher purity and is more robust against disturbance. The average power proportions of the target and unwanted modes of the 25 emitters are 0.80 and 0.04 for $k_z = k_0$ (0.85 and 0.04 for $k_z = -k_0$), respectively. The corresponding extinction ratio increases to 19 (20) in the case of $k_z = k_0$ ($k_z = -k_0$). And the purity of target OAM modes exhibits a standard deviation of 0.06 for $\ell = +2$ and 0.03 for $\ell = -2$.

Discussion and conclusion—In summary, by lifting the degeneracy of the $\mathrm{OAM}_{\pm\ell}$ modes with the OOI interaction in an on-chip chiral optical waveguide, we have theoretically predicted and experimentally observed OAM-momentum locking. The OAM vortex light beam can be generated with purity > 0.70 robust against various fabrication defects. The purity may be further improved by optimizing the photonic circuits.

This OAM-momentum locking provides a basis for expanding the boundaries of chiroptics [53] and chiral quantum optics [1] to high dimension on a chip. By combining with single-photon OAM emitters, the chiral optical waveguide may enable high-dimensional and topological Hong-Ou-Mandel interference [54] in a chip. It can also be used for on-chip generation of entangled OAM vortex beams. Thus, the demonstrated ℓ-selected OAM emitter offers a valuable platform and an appealing route for integrated high-dimensional topological information processing.

Acknowledgments—This research work was supported by the National Key R&D Program of China (Grants No. 2024YFA1409300, No. 2019YFA0706302, No. 2017YFA0308700, and No. 2019YFA0308703), the National Natural Science Foundation of China (Grants No. 62235012, No. 11904299 No. 61734005, No. 11761141014, No. 11690033, No. 12104299, No. 12304342, No. 92365107, No. 11890704, No. 12004166, No. 12574549, and No. 12574542), the Frontier Technologies R&D Program of Jiangsu (Grant No. SBF20250000094), the Innovation Program for Quantum Science and Technology (Grants No. 2021ZD0301400, No. 2021ZD0301500, and No. 2021ZD0300700), the Science and Technology Commission of Shanghai Municipality (STCSM) (Grants No. 20JC1416300, No. 2019SHZDZX01, No. 21ZR1432800, No. 22QA1404600, No. 24ZR1438700, No. 24ZR1430700, and No. 24LZ1401500), and the Shanghai Municipal Education Commission (SMEC) (Grant No. 2017-01-07-00-02-E00049). X.-M. J. acknowledges additional support from a Shanghai talent program and support from Zhiyuan Innovative Research Center of Shanghai Jiao Tong University. K. X. also thanks the support of Program for Innovative Talents and Entrepreneurs in Jiangsu (Grant No. JSSCTD202138). This work was also supported by Guangdong Provincial Natural Science Foundation (2019A1515110240). C.-W. Q. acknowledges the financial support by the Ministry of Education, Republic of Singapore (Grants No. A-8002152-00-00 and No. A-8002458-00-00), A*STAR IRG (M22K2c0088), and the Competitive Research Program Award (NRF-CRP26-2021-0004 and NRFCRP30-2023-0003) from the National Research Foundation, Prime Minister's Office, Singapore. Agency for Science, Technology and Research.

K. X., K.-D. Z., and X.-M. J. supervised the whole project and conceived the original idea. M.-Y. C., C.-W. Q., Y.-Q. L., and K. X. constructed the theoretical model. H.-M. W., Y. C., Y.-Y. F., K.-D. Z., and X.-M. J. performed the experiment and analyzed the data. M.-Y. C., C.-W. Q.,

Y.-Q. L., K. X., and X.-M. J. contributed to the mechanism underlying OAM-momentum locking. All authors contributed to writing the paper and discussion of physics.

Data availability—The data are not publicly available. The data are available from the authors upon reasonable request.

[1] P. Lodahl, S. Mahmoodian, S. Stobbe, A. Rauschenbeutel, P. Schneeweiss, J. Volz, H. Pichler, and P. Zoller, Chiral quantum optics, Nature (London) **541**, 473 (2017).

[2] K. Y. Bliokh, F. J. Rodríguez-Fortuño, F. Nori, and A. V. Zayats, Spin–orbit interactions of light, Nat. Photonics **9**, 796 (2015).

[3] K. Y. Bliokh, D. Smirnova, and F. Nori, Quantum spin Hall effect of light, Science **348**, 1448 (2015).

[4] K. Xia, G. Lu, G. Lin, Y. Cheng, Y. Niu, S. Gong, and J. Twamley, Reversible nonmagnetic single-photon isolation using unbalanced quantum coupling, Phys. Rev. A **90**, 043802 (2014).

[5] L. Tang, J. Tang, W. Zhang, G. Lu, H. Zhang, Y. Zhang, K. Xia, and M. Xiao, On-chip chiral single-photon interface: Isolation and unidirectional emission, Phys. Rev. A **99**, 043833 (2019).

[6] M. J. Mehrabad, A. P. Foster, R. Dost, E. Clarke, P. K. Patil, A. M. Fox, M. S. Skolnick, and L. R. Wilson, Chiral topological photonics with an embedded quantum emitter, Optica **7**, 1690 (2020).

[7] D. Smirnova, D. Leykam, Y. Chong, and Y. Kivshar, Nonlinear topological photonics, Appl. Phys. Rev. **7**, 021306 (2020).

[8] R. J. Coles, D. M. Price, J. E. Dixon, B. Royall, E. Clarke, P. Kok, M. S. Skolnick, A. M. Fox, and M. N. Makhonin, Chirality of nanophotonic waveguide with embedded quantum emitter for unidirectional spin transfer, Nat. Commun. **7**, 1 (2016).

[9] S. Luo, L. He, and M. Li, Spin-momentum locked interaction between guided photons and surface electrons in topological insulators, Nat. Commun. **8**, 2141 (2017).

[10] Y. Ma, H. Zhao, N. Liu, Z. Gao, S. S. Mohajerani, L. Xiao, J. Hone, L. Feng, and S. Strauf, On-chip spin-orbit locking of quantum emitters in 2d materials for chiral emission, Optica **8**, 953 (2022).

[11] G. Tkachenko and E. Brasselet, Optofluidic sorting of material chirality by chiral light, Nat. Commun. **5**, 3577 (2014).

[12] O. Hosten and P. Kwiat, Observation of the spin Hall effect of light via weak measurements, Science **319**, 787 (2008).

[13] T. V. Mechelen and Z. Jacob, Universal spin-momentum locking of evanescent waves, Optica **3**, 118 (2016).

[14] L. Peng, L. Duan, K. Wang, F. Gao, L. Zhang, G. Wang, Y. Yang, H. Chen, and S. Zhang, Transverse photon spin of bulk electromagnetic waves in bianisotropic media, Nat. Photonics **13**, 878 (2019).

[15] M. Wang, G. Hu, S. Chand, M. Cotrufo, Y. Abate, K. Watanabe, T. Taniguchi, G. Grosso, C.-W. Qiu, and A. Alù, Spin-orbit-locked hyperbolic polariton vortices carrying reconfigurable topological charges, eLight **2**, 12 (2022).

[16] A. V. Kavokin, G. Malpuech, and M. M. Glazov, Optical spin Hall effect, Phys. Rev. Lett. **95**, 136601 (2005).

[17] X. Yin, Z. Ye, J. Rho, Y. Wang, and X. Zhang, Photonic spin Hall effect at metasurfaces, Science **339**, 1405 (2013).

[18] Z. Shao, J. Zhu, Y. Chen, Y. Zhang, and S. Yu, Spin-orbit interaction of light induced by transverse spin angular momentum engineering, Nat. Commun. **9**, 926 (2018).

[19] M. Scheucher, A. Hilico, E. Will, J. Volz, and A. Rauschenbeutel, Quantum optical circulator controlled by a single chirally coupled atom, Science **354**, 1577 (2016).

[20] J.-S. Tang, W. Nie, L. Tang, M. Chen, X. Su, Y. Lu, F. Nori, and K. Xia, Nonreciprocal single-photon band structure, Phys. Rev. Lett. **128**, 203602 (2022).

[21] F. J. Rodríguez-Fortuño, G. Marino, P. Ginzburg, D. O'Connor, A. Martínez, G. A. Wurtz, and A. V. Zayats, Near-field interference for the unidirectional excitation of electromagnetic guided modes, Science **340**, 328 (2013).

[22] J. Petersen, J. Volz, and A. Rauschenbeutel, Chiral nanophotonic waveguide interface based on spin-orbit interaction of light, Science **346**, 67 (2014).

[23] S.-H. Gong, F. Alpeggiani, B. Sciacca, E. C. Garnett, and L. Kuipers, Nanoscale chiral valley-photon interface through optical spin-orbit coupling, Science **359**, 443 (2018).

[24] K. Rong, B. Wang, A. Reuven, E. Maguid, B. Cohn, V. Kleiner, S. Katznelson, E. Koren, and E. Hasman, Photonic Rashba effect from quantum emitters mediated by a Berry-phase defective photonic crystal, Nat. Nanotechnol. **15**, 927 (2020).

[25] X. Qiao, B. Midya, Z. Gao, Z. Zhang, H. Zhao, T. Wu, J. Yim, R. Agarwal, N. M. Litchinitser, and L. Feng, Higher-dimensional supersymmetric microlaser arrays, Science **372**, 403 (2021).

[26] Z. Zhang, H. Zhao, S. Wu, T. Wu, X. Qiao, Z. Gao, R. Agarwal, S. Longhi, N. M. Litchinitser, L. Ge, and L. Feng, Spin-orbit microlaser emitting in a four-dimensional Hilbert space, Nature (London) **612**, 246 (2022).

[27] P. Coullet, L. Gil, and F. Rocca, Optical vortices, Opt. Commun. **73**, 403 (1989).

[28] L. Allen, M. W. Beijersbergen, R. J. C. Spreeuw, and J. P. Woerdman, Orbital angular momentum of light and the transformation of Laguerre-Gaussian laser modes, Phys. Rev. A **45**, 8185 (1992).

[29] M. Erhard, R. Fickler, M. Krenn, and A. Zeilinger, Twisted photons: New quantum perspectives in high dimensions, Light Sci. Appl. **7**, 17146 (2018).

[30] Y. Chen, S. Liu, Y. Lou, and J. Jing, Orbital angular momentum multiplexed quantum dense coding, Phys. Rev. Lett. **127**, 093601 (2021).

[31] X.-L. Wang, Y.-H. Luo, H.-L. Huang, M.-C. Chen, Z.-E. Su, C. Liu, C. Chen, W. Li, Y.-Q. Fang, X. Jiang, L. Li, J. Zhang, N.-L. Liu, C.-Y. Lu, and J.-W. Pan, 18-qubit entanglement with six photons' three degrees of freedom, Phys. Rev. Lett. **120**, 260502 (2018).

[32] M. Chen, J.-S. Tang, M. Cai, Y. Lu, F. Nori, and K.-Y. Xia, High-dimensional two-photon quantum controlled phase-flip gate, Phys. Rev. Res. **6**, 033004 (2024).

[33] Y. F. Yang, M. Y. Chen, F. P. Li, Y. P. Ruan, Z. X. Li, M. Xiao, H. Zhang, and K. Y. Xia, Scalable cyclic transformation of orbital angular momentum modes based on

a nonreciprocal Mach-Zehnder interferometer, arXiv:2404.14690.

[34] Y. Zhang, M. Agnew, T. Roger, F. S. Roux, T. Konrad, D. Faccio, J. Leach, and A. Forbes, Simultaneous entanglement swapping of multiple orbital angular momentum states of light, Nat. Commun. **8**, 632 (2017).

[35] X. Ouyang, Y. Xu, M. Xian, Z. Feng, L. Zhu, Y. Cao, S. Lan, B.-O. Guan, C.-W. Qiu, M. Gu, and X. Li, Synthetic helical dichroism for six-dimensional optical orbital angular momentum multiplexing, Nat. Photonics **15**, 901 (2021).

[36] H. Sroor, Y. W. Huang, B. Sephton, D. Naidoo, V. Ginis, C. W. Qiu, A. Ambrosio, F. Capasso, and A. Forbes, High-purity orbital angular momentum states from a visible metasurface laser, Nat. Photonics **14**, 498 (2020).

[37] C.-W. Qiu and Y. Yang, Vortex generation reaches a new plateau, Science **357**, 645 (2017).

[38] X. Cai, J. Wang, M. J. Strain, B. Johnson-Morris, J. Zhu, M. Sorel, J. L. O'Brien, M. G. Thompson, and S. Yu, Integrated compact optical vortex beam emitters, Science **338**, 363 (2012).

[39] X. Zhang, Y. Liu, J. Han, Y. Kivshar, and Q. Song, Chiral emission from resonant metasurfaces, Science **377**, 1215 (2022).

[40] H. Ren, X. Li, Q. Zhang, and M. Gu, On-chip noninterference angular momentum multiplexing of broadband light, Science **352**, 805 (2016).

[41] Z. Zhang, X. Qiao, B. Midya, K. Liu, J. Sun, T. Wu, W. Liu, R. Agarwal, J. M. Jornet, S. Longhi, N. M. Litchinitser, and L. Feng, Tunable topological charge vortex microlaser, Science **368**, 760 (2020).

[42] B. Bahari, L. Hsu, S. H. Pan, D. Preece, A. Ndao, A. El Amili, Y. Fainman, and B. Kanté, Photonic quantum Hall effect and multiplexed light sources of large orbital angular momenta, Nat. Phys. **17**, 700 (2021).

[43] L. Rego, K. M. Dorney, N. J. Brooks, Q. L. Nguyen, C.-T. Liao, J. S. Román, D. E. Couch, A. Liu, E. Pisanty, M. Lewenstein, L. Plaja, H. C. Kapteyn, M. M. Murnane, and C. H.-García, Generation of extreme-ultraviolet beams with time-varying orbital angular momentum, Science **364**, eaaw9486 (2019).

[44] H. Pichler, T. Ramos, A. J. Daley, and P. Zoller, Quantum optics of chiral spin networks, Phys. Rev. A **91**, 042116 (2015).

[45] S. Mahmoodian, P. Lodahl, and A. S. Sørensen, Quantum networks with chiral-light–matter interaction in waveguides, Phys. Rev. Lett. **117**, 240501 (2016).

[46] Y. Chen, K.-Y. Xia, W.-G. Shen, J. Gao, Z.-Q. Yan, Z.-Q. Jiao, J.-P. Dou, H. Tang, Y.-Q. Lu, and X.-M. Jin, Vector vortex beam emitter embedded in a photonic chip, Phys. Rev. Lett. **124**, 153601 (2020).

[47] D. L. P. Vitullo, C. C. Leary, P. Gregg, R. A. Smith, D. V. Reddy, S. Ramachandran, and M. G. Raymer, Observation of interaction of spin and intrinsic orbital angular momentum of light, Phys. Rev. Lett. **118**, 083601 (2017).

[48] C. C. Leary and K. H. Smith, Unified dynamics of electrons and photons via Zitterbewegung and spin-orbit interaction, Phys. Rev. A **89**, 023831 (2014).

[49] See Supplemental Material at http://link.aps.org/supplemental/10.1103/tttd-v936, which includes Refs. [47,48,50,51], for relevant references on device design and calculations related to perturbed waveguides.

[50] Y. Chen, J. Gao, Z.-Q. Jiao, K. Sun, W.-G. Shen, L.-F. Qiao, H. Tang, X.-F. Lin, and X.-M. Jin, Mapping twisted light into and out of a photonic chip, Phys. Rev. Lett. **121**, 233602 (2018).

[51] Y. Wang, L. Zhong, K. Y. Lau, X. Han, Y. Yang, J. Hu, S. Firstov, Z. Chen, Z. Ma, L. Tong, K. S. Chiang, D. Tan, and J. Qiu, Precise mode control of laser-written waveguides for broadband, low-dispersion 3D integrated optics, Light Sci. Appl. **13**, 130 (2024).

[52] A. V. Dooghin, N. D. Kundikova, V. S. Liberman, and B. Ya. Zel'dovich, Optical Magnus effect, Phys. Rev. A **45**, 8204 (1992).

[53] Y. Chen, W. Du, Q. Zhang, O. Ávalos-Ovando, J. Wu, Q.-H. Xu, N. Liu, H. Okamoto, A. O. Govorov, Q. Xiong, and C.-W. Qiu, Multidimensional nanoscopic chiroptics, Nat. Rev. Phys. **4**, 113 (2022).

[54] M. Ehrhardt, C. Dittel, M. Heinrich, and A. Szameit, Topological Hong-Ou-Mandel interference, Science **384**, 1340 (2024).